*Journal of Applied Fluid Mechanics*, Vol. 19, No. 1, pp. 3444-3459, 2026. Available online at <a href="www.jafmonline.net">www.jafmonline.net</a>, ISSN 1735-3572, EISSN 1735-3645. <a href="https://doi.org/10.47176/jafm.19.1.3542">https://doi.org/10.47176/jafm.19.1.3542</a>



# Internal Flow Characteristics and Aerodynamic Noise Suppression of Serrated Trailing Edge Rotor Blades in an Axial-flow Turbine

D. D. Sui<sup>1,2</sup>, W. J. Yang <sup>1,3,4†</sup>, X. P. Wang<sup>1</sup>, Y. H. Wang<sup>1</sup>, and Y. Z. Zhang<sup>1</sup>

School of Mechatronics Engineering, Shenyang Aerospace University, Liaoning, Shenyang, 110136, China
 Nanjing Aviation Power Company Limited, Aero Engine Corporation of China, Jiangsu, Nanjing, 211153, China
 Key Laboratory of Rapid Development and Manufacturing Technology for Aircraft, Ministry of Education, Liaoning, Shenyang, 110136, China

†Corresponding Author Email: ncywj@sau.edu.cn

### **ABSTRACT**

The effects of rotor-stator interactions induce complex wake disturbances in turbine blades, and the use of a serrated trailing edge (STE) has been recognized as an effective flow control strategy. In this study, STEs were applied to the rotor blades of an AACHEN 1.5-stage axial-flow turbine, and it was to investigate the impact of the STEs on the aerodynamic and acoustic performance. Detached eddy simulation (DES) was employed to analyze the internal flow characteristics for different serration configurations. The results indicated that an STE could effectively improve the wake velocity of the rotor blade. The growth rate of the wake velocity reached 40.18% at the serration tip and 21.23% at the serration root, indicating improvements throughout the serrated region. Additionally, the STE rotor blades enhanced the flow mixing and generated rotational vortex structures between the serration peaks and valleys while maintaining the original aerodynamic performance. These vortices facilitated energy exchange between low-speed and high-speed regions, thereby reducing the wake vortex intensity. Furthermore, pressure fluctuations were effectively suppressed by the effect of the STE rotor blades, leading to a significant noise reduction, with the sound pressure level (SPL) reduced by approximately 8.52 dB in the low-frequency range and 12.49 dB in the high-frequency range. These findings confirmed that the STE blade improved both aerodynamic and acoustic characteristics. Thus, this study provides valuable insights for turbine blade design optimization and noise reduction strategies.

### Article History

Received March 24, 2025 Revised August 15, 2025 Accepted August 29, 2025 Available online November 5, 2025

#### **Keywords:**

Turbine blade Serrated trailing edge Vortex structures Noise suppression Flow control

# 1. Introduction

The continuous advancement of turbine technology is a significant driving force for innovation and sustainable development in the aviation industry. In axial turbines, the periodic interaction between rotor and stator blades induces strong unsteady flows. Under high-load conditions, complex vortices are generated by the interactions between the potential field and wake shear of the rotor and stator blades. The formation, convection, and dissipation of these vortices directly influence wake disturbances, which serve as primary sources of aerodynamic noise. The spatiotemporal evolution of these disturbances is closely linked to the noise spectrum.

Extensive research has been conducted to analyze the impact of the turbulence-related effects induced by wakes for turbine blades on unsteady flow development, boundary layer transitions, and aerodynamic losses. Hodson & Howell (2005a, b) investigated the unsteady flow evolution in low-pressure turbines, with a focus on wake-induced boundary layer transitions and the associated loss mechanisms. Wissink et al. (2006) examined the influence of periodic wake disturbances on the separated flows around turbine blades, and the researchers described the interaction between wakes and boundary layer development. Meyer (1958) identified velocity deficits as a key characteristic of the wakes generated by upstream blade rows, describing the wakes as reverse jets with velocity components opposite to the mainstream flow, a phenomenon known as reverse flow.

<sup>&</sup>lt;sup>4</sup> State Key Laboratory for Aviation Digital Manufacturing Process, Shenyang Aerospace University, Liaoning, Shenyang, 110136, China

NOMENCLATURE						
N-S	Navier-Stokes	P	velocity growth rate			
RANS	Reynolds-Averaged Navier-Stokes	$\nu$	minimum wake velocities for the STE blade			
CFD	Computational Fluid Dynamics	$v_{ m o}$	minimum wake velocities for the baseline blade			
EXP	Experimental	STE	Serrated Trailing Edge			
DES	Detached Eddy Simulation	$\Pi_t$	turbine expansion ratio			
LES	Large Eddy Simulation	ṁ	mass flow			
S	height of rotor blade	Q	Q-criterion			
C	chord length of rotor blade	BPF	Blade Passing Frequency			
h	serration height	FFT	Fast Fourier Transform			
λ	serration width	SPL	Sound Pressure Level			
$\eta_{ m s}$	isentropic efficiency	CAA	Computational Aeroacoustics			

flow. As wakes propagate into downstream blade passages, they are sheared by the leading edge of the blades, forming independent wake segments. Each segment behaves as a reverse jet that promotes fluid transport from the pressure side to the suction side and alters the pressure and velocity distributions on the blade surface. The transport of wakes within turbine blade passages is governed by complex mechanisms, including wake cutting, bending, stretching, and deformation. All of these mechanisms significantly influence the aerodynamic loading characteristics of turbine blades (Yildiz et al., 2024; Liu et al., 2022; Hu et al., 2019; Li et al., 2024).

Many researchers have investigated innovative blade designs and optimization strategies to enhance the performance aerodynamic and efficiency turbomachinery across various operating conditions. Chen et al. (2018) proposed a bifurcated blade design based on pressure gradient control. The design incorporated variable solidity and three-dimensional blade shaping to suppress secondary flow migration in the endwall region of compressor blades. This design effectively mitigated wall separation and wake losses, leading to a significant improvement in aerodynamic performance. Manabe et al. (2019) introduced an optimization framework that integrated aerodynamic design methodologies with genetic algorithms to simultaneously optimize the blade loading distribution and meridional geometry of centrifugal compressors. The optimized significantly enhanced the total pressure ratio and adiabatic efficiency under low-flow conditions while suppressing boundary layer development near the shroud. Yuan et al. (2024) applied tandem blade technology to a transonic ultra-highly loaded axial compressor and replaced the conventional single-blade rotor with a tandem rotor to evaluate its effects on compressor performance and aerodynamic loading. The results indicated that the optimized tandem rotor configuration achieved a 0.83% increase in the peak efficiency, a 2.16% improvement in the stall margin, and a 0.30% enhancement in the choke flow rate. Rona & Gostelow (2005) demonstrated that rear edge blowing and slotted tailboards, when properly configured, could effectively regulate blade wake dynamics, improving overall blade flow characteristics.

With advancements in blade biomimicry, the natural serrated characteristics of wing trailing edges have attracted significant research attention. Howe (1991) was among the first to analyze the aerodynamic and acoustic effects of trailing-edge serrations, demonstrating their

direct influence on aerodynamic noise and flow characteristics. Subsequently, Ahmadkhah et al. (2025) investigated the effect of different trailing-edge serration designs on the aerodynamic performance of a wing-flap system, with consideration of sinusoidal, square, and triangular serration shapes. Numerical simulations revealed that all of the serrated configurations contributed to drag reduction and lift enhancement, with the sinusoidal serrations exhibiting the best overall performance. Feng et al. (2023) applied STEs to horizontal-axis wind turbine blades to mitigate aerodynamic noise. Their findings showed a 6.9 dB reduction in the sound pressure level (SPL) in the mid-to-high frequency range. Additionally, the wake vortex shedding intensity was reduced, and the vortex interactions were weakened, indicating the effective suppression of vortex-induced noise. Lee et al. (2021) and Ye et al. (2022a) analyzed the flow characteristics of STEs, demonstrating their ability to suppress boundary layer flow separation, minimize flow losses, and improve vortex structures. Yang et al. (2025a, b) explored the rotor-stator interaction and introduced non-uniform serrations at the trailing edge of a stator blade trailing edge, effectively improving the wake profile. This design enhanced mixing between the main flow and wake region, reduced velocity deficits, and improved both efficiency and operating stability in a transonic compressor. To quantitatively evaluate aerodynamic noise, related researchers (Ye et al., 2022b; Kim et al., 2021; Li et al., 2020; Liu et al., 2019) obtained the nearfield pulsating pressures from simulations or experiments, then they were transformed into SPL spectra using Fast Fourier Transform (FFT) (Ghasemian & Nejat, 2015) to identify dominant noise sources such as vortex shedding and blade passing frequency. Their results confirmed that serrated structures significantly reduced the noise generated by periodic wake interactions between stator and rotor blades, as well as potential field interactions between the two. With the growing understanding of serrated flow fields, these types of designs have been widely implemented for noise reduction in various applications, including wings, wind turbine blades, and other trailing-edge configurations (Chong & Vathylakis, 2015; Alawadhi et al., 2014; Chandra & Sharma, 2017; Naeini et al., 2019).

In this study, the applications of STE rotor blades were investigated. STE rotor blades are significantly different from conventional stator STEs due to the strong rotor-stator interactions caused by the rotational speed. The DES method was employed to analyze the internal

flow characteristics for different serration configurations. The effects of rotor-based STEs were discussed with respect to wake velocity deficits and flow mixing. Furthermore, the suppression of aerodynamic noise was analyzed based on the aerodynamic performance and flow characteristics. The goal of this study was to provide valuable insights into aerodynamic optimization and noise reduction strategies for STE blades.

# 2. RESEARCH OBJECTS AND NUMERICAL METHODS

# 2.1 A Numerical Model of an Aachen Turbine Cascade

A 1.5-stage axial turbine was selected as the research object in this study. The turbine was developed by the Institute of Jet Propulsion and Turbomachinery at RWTH Aachen University, Germany (Maciej & Blaszczak, 2008). The turbine's structure is shown in Fig. 1, and the relevant design parameters are summarized in Table 1. The turbine stage was composed of a stator-rotor-stator configuration, with all blades being untwisted. The second stator shared the same airfoil profile, stagger angle, and blade count as the first stator. The tip clearance of the rotor blades was 0.4 mm.



Fig. 1 A model of an Aachen 1.5-stage turbine

**Table 1 Turbine cascade parameters** 

	Values		
Parameters	1st and 2nd		
	stators	Rotor	
Number of blades	36	41	
Rotational speed/rpm	-	3500	
Reynolds number	$6.8 \times 10^{5}$	4.9×10 <sup>5</sup>	
Tip clearance/mm	-	0.4	
Aspect ratio	0.887	0.917	
Tip diameter/mm	600	599.2	
Hub diameter/mm	490	490	
Passage height/mm	55	55	
Flow angle α/°	20	90	
Relative flow angle $\beta$ /°	49.3	151.2	

A numerical model of the turbine's flow field is illustrated in Fig. 2. Under the design conditions, the turbine operated at a rotational speed of 3500 rpm, with an inlet static pressure of 153700 Pa. The total temperature at the inlet was maintained within 308K  $\pm$  0.5 K, while the outlet backpressure was set to 134209 Pa. Additionally, the data exchange between the rotor and stator blades was achieved with the sliding mesh interface.

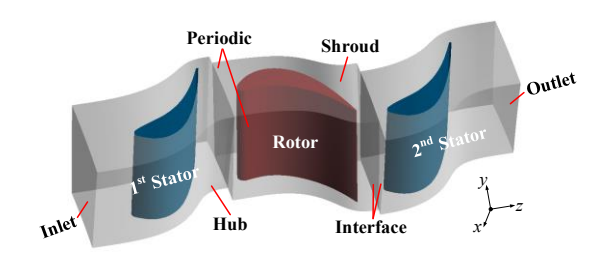


Fig. 2 Flow field of turbine cascade

Accurate mesh generation is essential for capturing fluid behavior in computational fluid dynamics (CFD) simulations. Three mesh densities were established in this study, as summarized in Table 2. Figure 3 presents a threedimensional view of the computational domain and its topological details under the fine-mesh configuration. Htype and O-type mesh topologies were applied near the blade surfaces. For the fine-mesh simulation, the computational domain was discretized into 2.35×106 nodes, with the number of grid points in each spatial direction approximately tripled compared to the coarse mesh. Near the blade walls, the first cell height was chosen to ensure a dimensionless wall distance of y<sup>+</sup><1. A total of 20 layers were clustered near the blade surfaces with geometrically increasing thickness to resolve boundary layer gradients. In critical regions such as the wake and shear layers, finer cells were employed to precisely capture vortices and pressure fluctuations. Away from the blades, the cell sizes gradually increased with controlled expansion ratios below 1.2 to avoid numerical diffusion and preserve solution accuracy.

Table 2 Three mesh density schemes

Grid	Elements			Total
scheme	1st stator	Rotor	2 <sup>nd</sup> stator	elements
Coarse	1.59×10 <sup>5</sup>	4.41×10 <sup>5</sup>	2.22×10 <sup>5</sup>	8.23×10 <sup>5</sup>
Medium	2.81×10 <sup>5</sup>	8.05×10 <sup>5</sup>	3.79×10 <sup>5</sup>	1.59×10 <sup>6</sup>
Fine	4.42×10 <sup>5</sup>	1.32×10 <sup>6</sup>	5.95×10 <sup>5</sup>	2.35×10 <sup>6</sup>

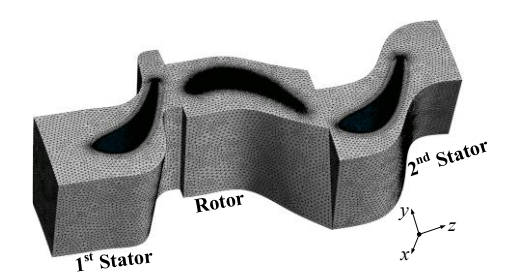


Fig. 3 Mesh of the computational flow field

The Reynolds-averaged Navier-Stokes (RANS) method was employed to solve the flow field, modeling the fluid motion within the turbine by solving the Navier-Stokes (N-S) equations (Launder, 1974). In the RANS formulation, the equations for mass, momentum, and energy conservation are considered separately in the x, y, and z directions. Additionally, Reynolds stress terms are introduced to account for the additional stresses that are induced by turbulence. These equations are expressed as follows:

(i) The equation of mass conservation:

$$\frac{\partial \overline{\rho}}{\partial t} + \frac{\partial}{\partial x} \left( \overline{\rho u} \right) + \frac{\partial}{\partial y} \left( \overline{\rho v} \right) + \frac{\partial}{\partial z} \left( \overline{\rho w} \right) = 0 \tag{1}$$

(ii) The equation of momentum conservation:

$$\begin{bmatrix} \frac{\partial(\overline{\rho u})}{\partial t} + \frac{\partial(\overline{\rho u^2})}{\partial x} + \frac{\partial(\overline{\rho u w})}{\partial y} + \frac{\partial(\overline{\rho u w})}{\partial z} = -\frac{\partial \overline{p}}{\partial x} + \frac{\partial}{\partial x} \left[ \overline{\mu} \left( \frac{\partial \overline{u}}{\partial x} + \frac{\partial \overline{v}}{\partial y} + \frac{\partial \overline{w}}{\partial z} \right) - \overline{\rho u'v'} - \overline{\rho u'w'} \right] \\ \frac{\partial(\overline{\rho v})}{\partial t} + \frac{\partial(\overline{\rho u w})}{\partial x} + \frac{\partial(\overline{\rho v w})}{\partial y} + \frac{\partial(\overline{\rho v w})}{\partial z} = -\frac{\partial \overline{p}}{\partial y} + \frac{\partial}{\partial y} \left[ \overline{\mu} \left( \frac{\partial \overline{u}}{\partial x} + \frac{\partial \overline{v}}{\partial y} + \frac{\partial \overline{w}}{\partial z} \right) - \overline{\rho v'u'} - \overline{\rho v'w'} \right] \\ \frac{\partial(\overline{\rho w})}{\partial t} + \frac{\partial(\overline{\rho u w})}{\partial x} + \frac{\partial(\overline{\rho v w})}{\partial y} + \frac{\partial(\overline{\rho w w})}{\partial z} = -\frac{\partial \overline{p}}{\partial z} + \frac{\partial}{\partial z} \left[ \overline{\mu} \left( \frac{\partial \overline{u}}{\partial x} + \frac{\partial \overline{v}}{\partial y} + \frac{\partial \overline{w}}{\partial z} \right) - \overline{\rho w'u'} - \overline{\rho w'v'} \right] \end{aligned}$$

(iii) The equation of energy conservation:

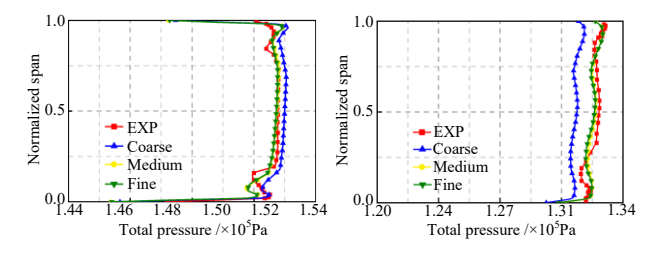
$$\frac{\partial(\overline{\rho E})}{\partial t} + \frac{\partial(\overline{\rho u E})}{\partial x} + \frac{\partial(\overline{\rho v E})}{\partial y} + \frac{\partial(\overline{\rho w E})}{\partial z} = \frac{\partial}{\partial x} \left[ \left( \overline{\lambda} + \frac{\overline{\mu} c_p}{Pr} \right) \frac{\partial \overline{T}}{\partial x} - \overline{\rho u' T'} \right] + \frac{\partial}{\partial y} \left[ \left( \overline{\lambda} + \frac{\overline{\mu} c_p}{Pr} \right) \frac{\partial \overline{T}}{\partial z} - \overline{\rho w' T'} \right] + \frac{\partial}{\partial z} \left[ \left( \overline{\lambda} + \frac{\overline{\mu} c_p}{Pr} \right) \frac{\partial \overline{T}}{\partial z} - \overline{\rho w' T'} \right]$$
(3)

In the governing equations,  $\bar{\rho}$  represents the timeaveraged density, indicating the mean mass per unit volume. The velocity components in the x, y, and zdirections are denoted as  $\overline{u}$ ,  $\overline{v}$ , and  $\overline{w}$ , respectively. The time-averaged pressure is given by  $\bar{p}$ , while  $\bar{\mu}$  represents the time-averaged dynamic viscosity, which characterizes the fluid's viscous properties. The Reynolds stress terms are noted as  $\overline{\rho u'v'}$ ,  $\overline{\rho u'w'}$ ,  $\overline{\rho v'u'}$ ,  $\overline{\rho v'w'}$ ,  $\overline{\rho w'u'}$ , and  $\overline{\rho w'v'}$ , and these terms account for the additional stresses induced by turbulence and describe the interactions between the velocity components.  $\overline{\rho E}$  denotes the timeaveraged total energy, including both internal energy and kinetic energy. The time-averaged temperature is denoted as  $\bar{T}$ . The term  $\bar{\lambda}$  represents the time-averaged thermal conductivity, describing the fluid's ability to conduct heat.  $C_p$  is the specific heat capacity at constant pressure, which quantifies the temperature increase of a unit mass of fluid under constant pressure. The Prandtl number  $P_r$  is defined as the ratio of the dynamic viscosity to the thermal conductivity and is applied to characterize the thermal transport properties of the fluid.

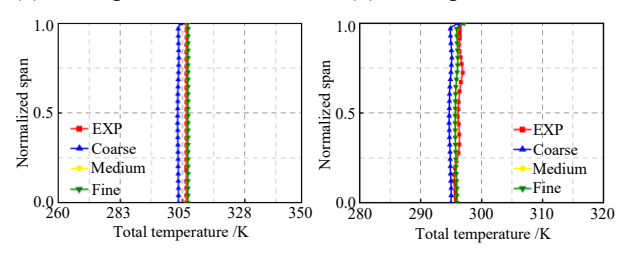
#### 2.2 Validation of Numerical Method

The steady-state numerical simulations were performed using ANSYS-CFX. Figure 4 presents a comparison between the CFD results and the experimental measurements (EXP), for which the EXP data were provided by Aubé & Hirsch (2001). The circumferentially averaged total pressure, total temperature, and flow angle 8.8 mm downstream of the first stator and rotor trailing edges were applied to validate the accuracy of the numerical method.

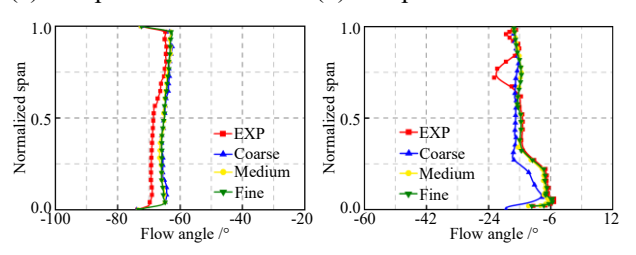
Figures 4(a) and 4(b) indicate that the medium and fine grids produced results closer to the EXP data compared to the coarse grid, demonstrating that the grid refinement enhanced the computational accuracy. Regarding the total temperature distribution, the CFD predictions exhibited good agreement with the EXP measurements, with minimal variation among different grid resolutions, suggesting that the total temperature predictions were relatively stable and less sensitive to the grid resolution. Moreover, in terms of the flow angle



(a) Total pressure of 1st stator (b) Total pressure of rotor



(c) Temperature of 1st stator (d) Temperature of rotor



(e) Flow angle of 1st stator

(f) Flow angle of rotor

Fig. 4 Comparison of the CFD result and EXP data

distribution, as shown in Fig. 4(e) and Fig. 4(f), significant deviations were observed in the coarse grid results, whereas the fine grid substantially improved the prediction accuracy. A comprehensive analysis revealed that the grid refinement effectively improved the accuracy of total pressure and flow angle predictions. Therefore, the discretized grid resolution in the fine-mesh configuration was confirmed to meet the accuracy requirements, allowing precise predictions of the circumferentially averaged total pressure, total temperature, and flow angle for both the stator and rotor.

To further validate the accuracy of the computational results, Fig. 5 presents the transient entropy distribution of the turbine blade at the 50% spanwise location, with the iso-contours of the CFD result compared to the EXP data (Walraevens et al., 1998). The results indicated good agreement between the CFD result and the EXP data, thereby confirming the reliability of the adopted numerical model and the computational methodology.

### 2.3 Flow Characteristic of the Baseline Blade

Figure 6 illustrates the expansion ratio-efficiency ( $\Pi_t$ - $\eta_s$ ) and expansion ratio-mass flow ( $\Pi_t$ - $\dot{m}$ ) characteristics of the turbine. Under the design conditions, a mass flow rate  $\dot{m}$ =8.33 kg/s, an efficiency of  $\eta_s$ =84.72%, and an expansion ratio of  $\Pi_t$ =1.19 were obtained. From the  $\Pi_t$ - $\eta_s$  curve, an increase in  $\eta_s$  was observed as  $\Pi_t$  rose, reaching a peak of  $\eta_s$ =85.89% at  $\Pi_t$ =1.12. Beyond this point, a further increase in  $\Pi_t$  resulted in a decline in  $\eta_s$ , although the rate of decrease was lower than the preceding rate of increase. Additionally, the design point was in the

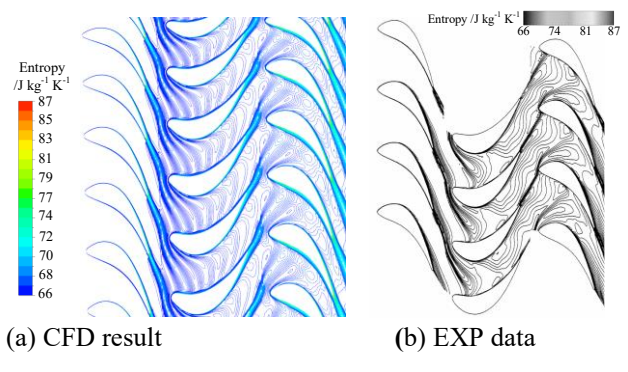


Fig. 5 Entropy distribution of the turbine at the 50% spanwise location

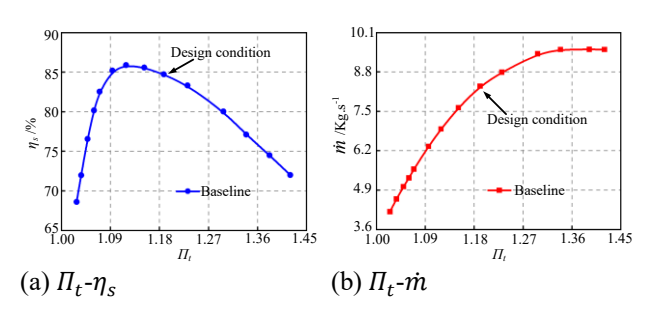


Fig. 6 Curves of turbine characteristic

efficiency decline region rather than at the peak efficiency. The  $\Pi_t$ - $\dot{m}$  curve indicated that  $\dot{m}$  increased with  $\Pi_t$  and gradually stabilized at  $\Pi_t$ =1.33, marking the onset of the critical expansion ratio region. At the design point,  $\dot{m}$  remained below the choking condition.

As shown in Fig. 7, three velocity monitoring lines were placed 4 mm downstream of the rotor blade trailing edge at the 20%, 50%, and 80% spanwise locations to capture the wake velocity distribution. Figure 8 illustrates the distribution characteristics of the wake velocity, revealing its periodic fluctuations with rotor operation. Additionally, an increase in the wake velocity with the spanwise height was observed, indicating significant differences in the wake disturbances between the blade rows.

Figure 9 illustrates the static pressure distribution along the streamlines at the 20%, 50%, and 80% spanwise locations on the baseline blade. A gradual decrease in the static pressure was induced by gas expansion on the pressure side, forming a pressure gradient, which was found to diminish along the spanwise direction. In the blade root region, the pressure difference between the pressure and suction sides remained small, while a rapid drop in the static pressure was observed near the trailing edge, indicating the strong influence of the geometric constraints and vortex effects. A significant pressure difference was detected at the trailing edge of the 80% spanwise location, and this difference was primarily caused by the tip leakage flow and secondary flow effects.

Unsteady calculations for the turbine were performed using the RANS method with a time step of  $4.20 \times 10^{-5}$  s, and transient rotor-stator interface conditions were applied. To reduce the numerical dissipation and accurately capture flow discontinuities, a second-order

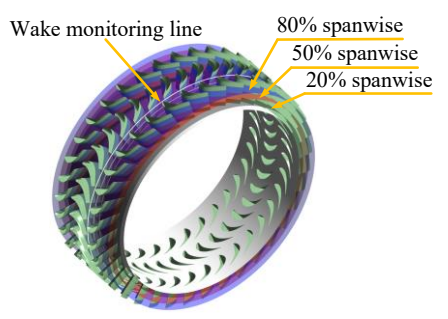


Fig. 7 Wake velocity monitoring lines at different spanwise

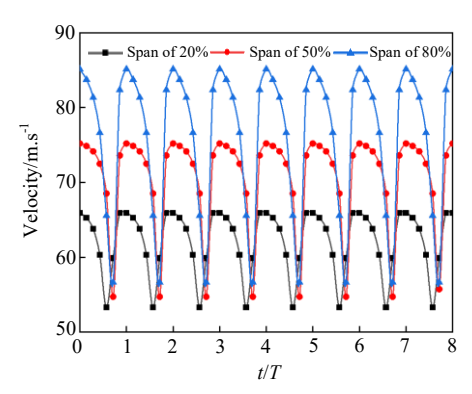


Fig. 8 Wake velocity distribution of the rotor at different spanwise locations

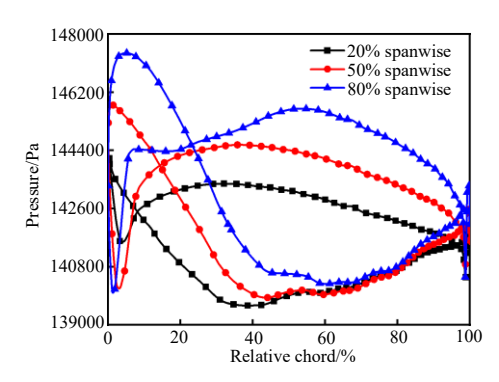


Fig. 9 Static pressure distribution of the baseline blade at different spanwise locations

implicit transient integration scheme was utilized. Figure 10 presents the static entropy distribution at four discrete time steps located at the 50% spanwise location of the turbine blade. These visualizations effectively captured the dynamics of the wake transport within the blade passage. At point A, low-energy fluid was generated at the stator trailing edge and was subsequently cut by the rotor blade leading edge due to the inter-stage interference effects, forming a distinct wake segment. At point B, the wake curvature was observed because the flow speed in the middle of the blade passage was higher than that near the blade leading edge. This curved wake entered the rotor passage, where the wake near the suction side was transported faster than that near the pressure side due to the higher velocity on the suction side. As a result, the lowenergy fluid near the pressure side moved toward the suction side, causing the wake segment to elongate and thin. At point C, the wake width increased near the suction side due to fluid accumulation.

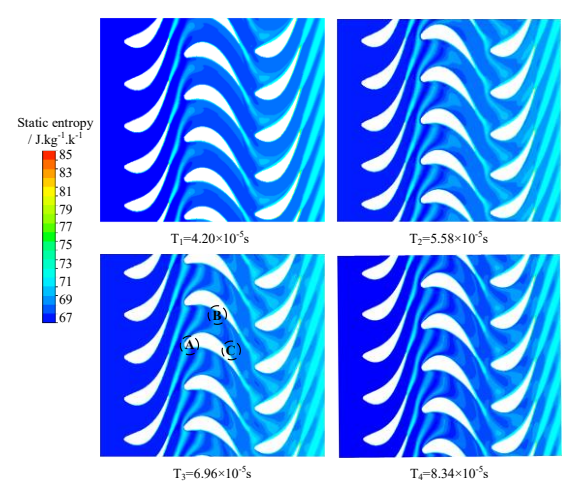


Fig. 10 Static entropy distributions of the turbine

# 3. FLOW CHARACTERISTICS OF STE BLADES

### 3.1 Structure of Bionic Serration

Biological systems serve as a significant source of inspiration for engineering design (Gruber et al., 2011) and offer strategies to enhance mechanical performance through biomimetic structures. As illustrated in Fig. 11, a serrated structure inspired by bird wings was incorporated into the turbine blade design. The rotor blade had a chord length of C=62 mm and a height of S=55 mm. The serrated configuration was primarily based on a triangular pattern, where h represents the serration height and  $\lambda$  denotes the serration width.

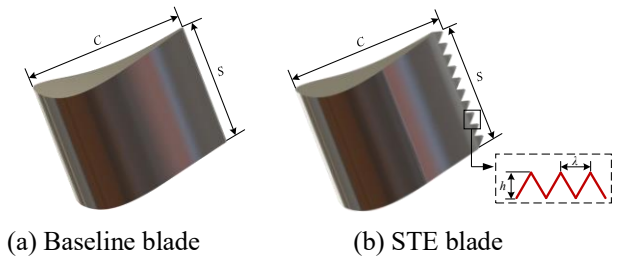
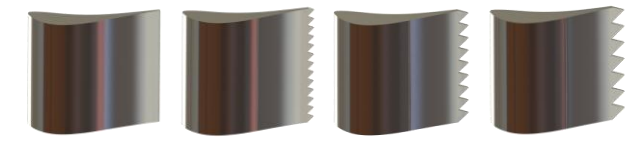


Fig. 11 Structures of the blade's trailing edge

# 3.2 Parameters of Serrations in the Blade's Trailing Edge

A series of STE blades with varying  $\lambda/C$  ratios was generated by scaling the serration dimensions while maintaining a constant ratio of  $h/\lambda=1$ . Specifically, the values of  $\lambda/C$  were set to remain unchanged, and the series of  $\lambda/C$  was set to 0.07, 0.10, and 0.13, corresponding to serration heights of 4.34 mm, 6.20 mm, and 8.06 mm, respectively. The serration width was equal to its corresponding height. The resulting STE blades with different  $\lambda/C$  configurations are illustrated in Fig. 12.

To investigate the influence of serrated structures on the internal flow, serrated rotor blades were implemented in the turbine and analyzed through CFD simulations. The three serration configurations corresponded to the serration tip and root at the 82% and 23% spanwise locations, respectively. As shown in Fig. 13, the data extraction line was positioned 0.3 mm downstream of the trailing edge.



(a) Baseline blade (b)  $\lambda/C=0.07$  (c)  $\lambda/C=0.10$  (d)  $\lambda/C=0.13$ 

Fig. 12 STE blades in different  $\lambda/C$  configurations

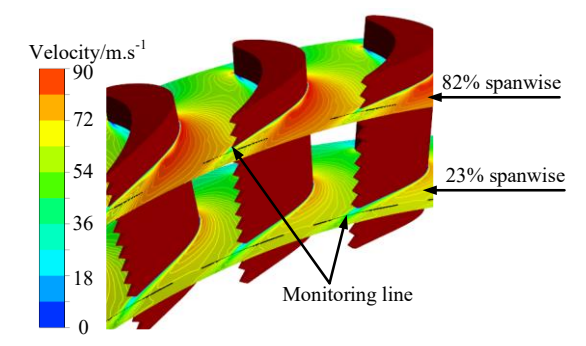


Fig. 13 Schematic of velocity monitoring lines

The wake velocity distributions of the baseline and STE blades are presented in Fig. 14(a) and Fig. 14(b). It can be observed from the figures that the STE blades mitigated the wake velocity loss, with the  $\lambda/C=0.10$  configuration exhibiting a smaller velocity difference between the freestream and wake regions at both the tip and root. Additionally, the influence of the serrations was more pronounced at the serration tips, likely due to the enhanced flow mixing in this region, which promoted the momentum exchange and reduced wake velocity deficits.

Figures 14(c) and Fig. 14(d) compare the wake velocity growth rate P for different serration configurations. The  $\lambda/C=0.10$  blade exhibited the highest performance, with a P value of 40.18% at the serration tip and 21.23% at the serration root, outperforming the other two STE blade configurations. The wake velocity growth rate P is calculated as follows:

$$P = \frac{v - v_o}{v_o} \times 100\%$$
 (4)

where  $v_0$  and v denote the minimum wake velocities for the baseline and STE blades.

Since the  $\lambda/C$ =0.10 exhibited a lower wake velocity loss along the same spanwise location, a series of STE blades with varying heights was developed while maintaining a constant serration width  $\lambda_0$ . The definition of  $\lambda/C$ =0.10 remained unchanged, resulting in serration configurations with  $h/\lambda_0$ =0.07,  $h/\lambda_0$ =0.10,  $h/\lambda_0$ =0.13, and  $h/\lambda_0$ =0.16. The models of these STE blades are illustrated in Fig. 15.

As shown in Fig. 16, the wake velocity profiles were extracted along monitoring lines at different spanwise locations. The results indicated that the STE blades effectively mitigated the wake velocity loss. At the 80% spanwise location, the  $h/\lambda_0$ =0.07 configuration exhibited a significantly lower velocity loss compared to the other cases. As the spanwise location percentage decreased, the differences in the wake velocity loss among the four serration configurations gradually diminished. This trend

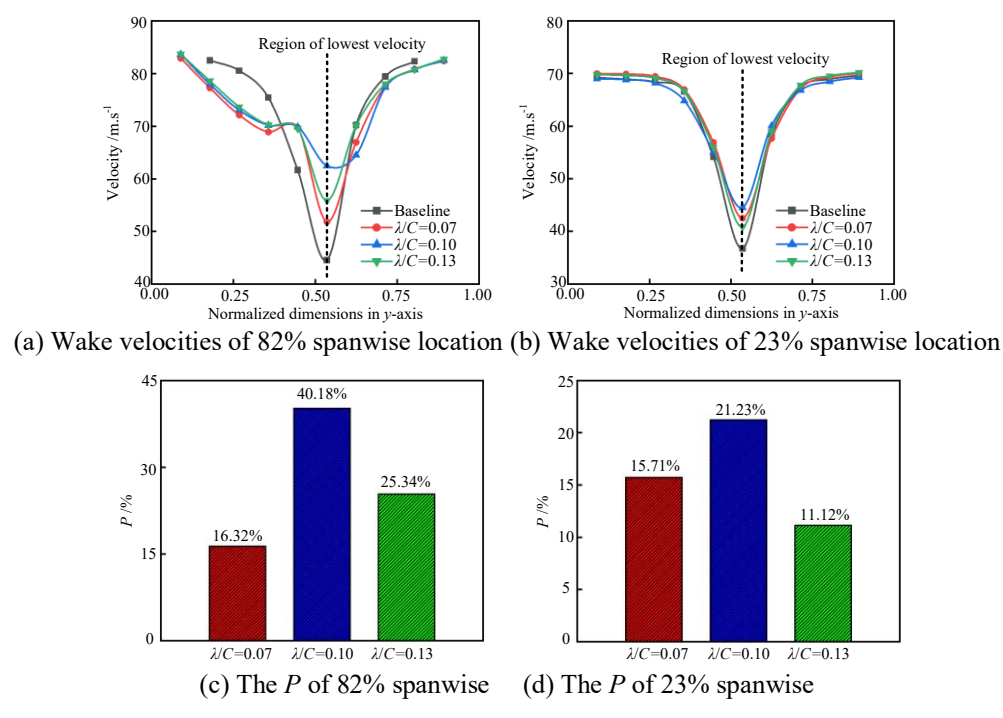


Fig. 14 Wake velocity distributions of different blades

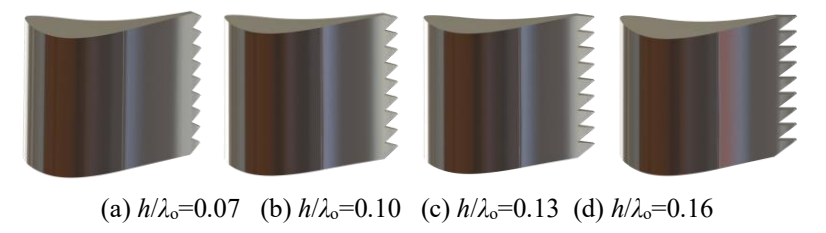


Fig. 15 STE blades in different  $h/\lambda_0$  configurations

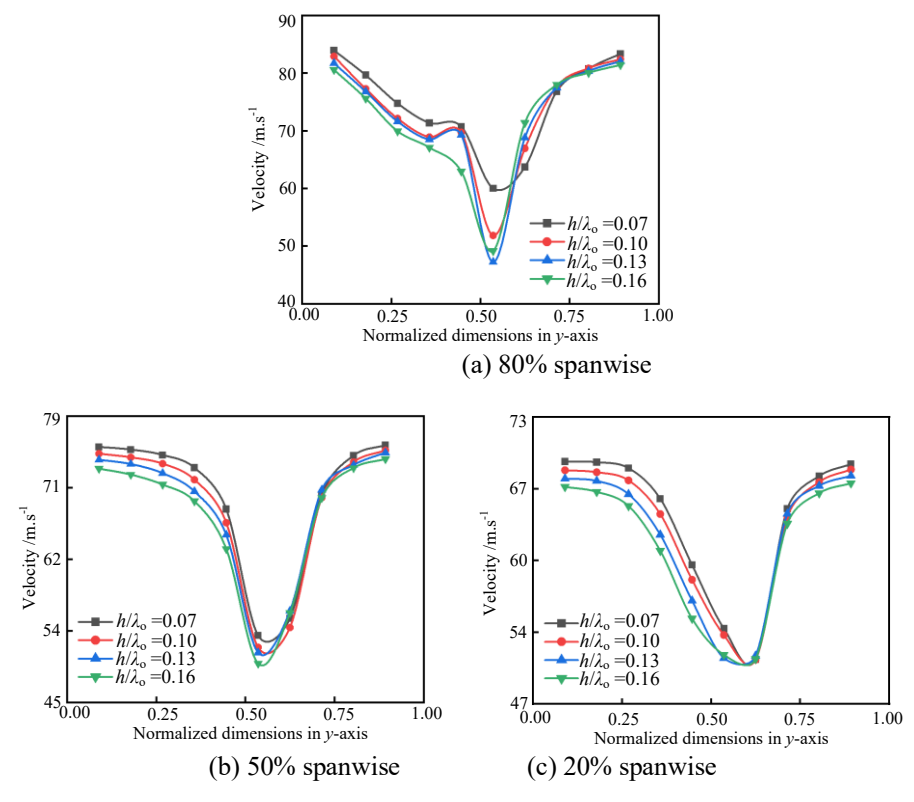


Fig. 16 Wake velocities of different STE blades

indicated that a smaller  $h/\lambda_o$  value resulted in reduced wake losses. This, in turn, suggested that the serration geometric parameters significantly influenced the wake characteristics. Based on these findings, the  $h/\lambda_o$ =0.07 serration configuration was selected for further application to the turbine rotor blade. Subsequently, the influence of the STE on the aerodynamic performance and the internal flow characteristics of an axial-flow turbine was further analyzed.

# 3.3 Aerodynamic performance and flow characteristics of the STE blade

Figure 17 illustrates the mesh distribution of the STE blade. The overall flow field was discretized using tetrahedral elements. The computational domain consisted of approximately  $2.62\times10^6$  elements. Near the blade surface, an H-type mesh refinement was applied to ensure sufficient resolution for capturing the geometric details of the STE while satisfying the mesh accuracy requirements specified in Section 2.1.

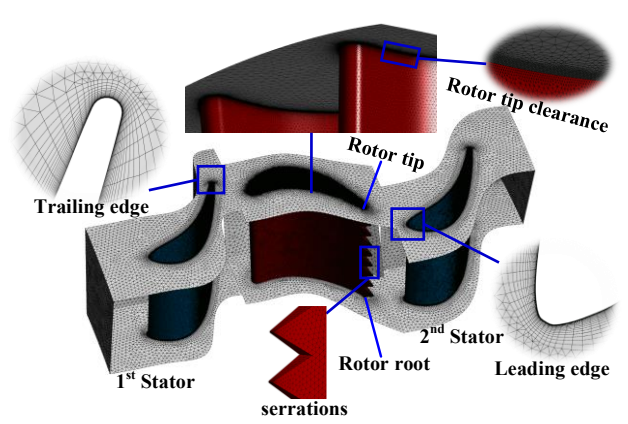


Fig. 17 Mesh of the STE blade

To ensure the accurate resolution of the complex flow structures induced by the STE, mesh refinement was applied near the serration regions. Figure 18 illustrates the mesh topology around the rotor blade. High-density grid clustering was visible near the trailing edge and serration tips. This localized refinement was implemented to capture the small-scale vortices and sharp geometric features introduced by the serration structures. A multiblock structured mesh strategy was employed, with

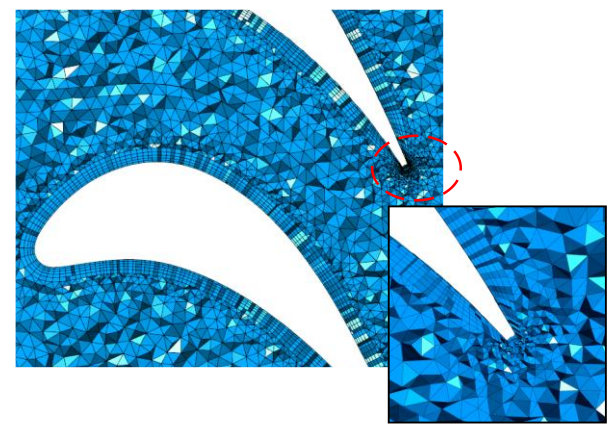
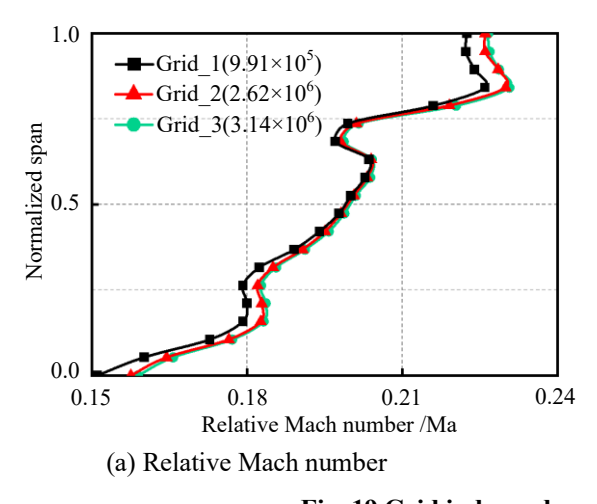


Fig. 18 Local refined mesh near the serration tip

smooth grid transitions used to maintain numerical stability and avoid artificial diffusion.

Figure 19 presents the results for a mesh independence study that was conducted at the rotor blade trailing edge using three mesh resolutions. This validation was performed by examining the spanwise distributions of the relative Mach number and the meridional velocity at the trailing edge. The results showed that Grid\_2 and Grid\_3 exhibited nearly identical profiles, whereas Grid\_1 showed noticeable deviations, particularly in the mid-span and tip regions. This comparison indicated that Grid\_2 achieved mesh independence, since further mesh refinement yielded negligible improvements. Therefore, Grid\_2 was selected for the subsequent simulations to ensure both accuracy and computational efficiency.

Figure 20 presents the residual convergence histories for both steady and unsteady computations. The residuals of the mass conservation equation (P-Mass) and momentum equations in the *x*, *y*, and *z* directions (U-Mom, V-Mom, W-Mom) are plotted in Fig. 20(a). During the steady-state simulation, all of the residuals exhibited a consistent downward trend, ultimately reaching values on the order of 10<sup>-4</sup>, indicating that the flow field had converged. Figure 20(b) shows the residual histories associated with the turbulence model, including the turbulence kinetic energy (K-TurbKE) and dissipation rate (E-Diss.K). In the transient simulation, these residuals



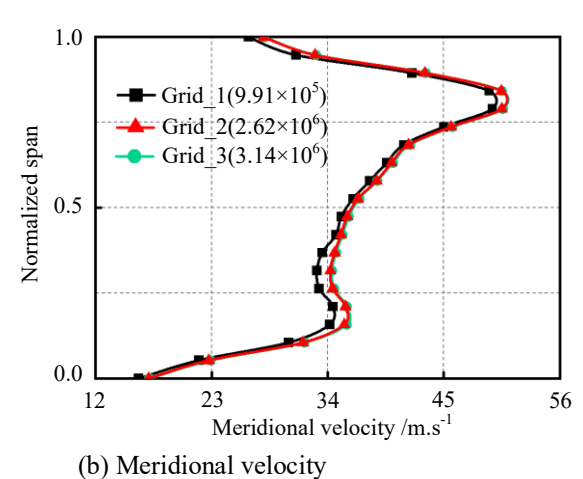
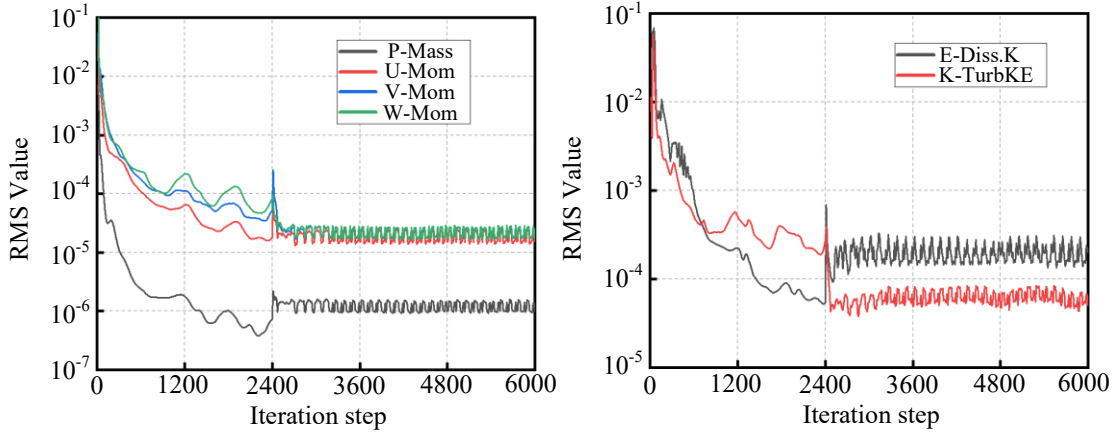


Fig. 19 Grid independence verification of STE blades



(a) RMS residuals of mass and momentum equations (b) RMS residuals of turbulence model equations

Fig. 20 Residual histories for the steady and transient simulations

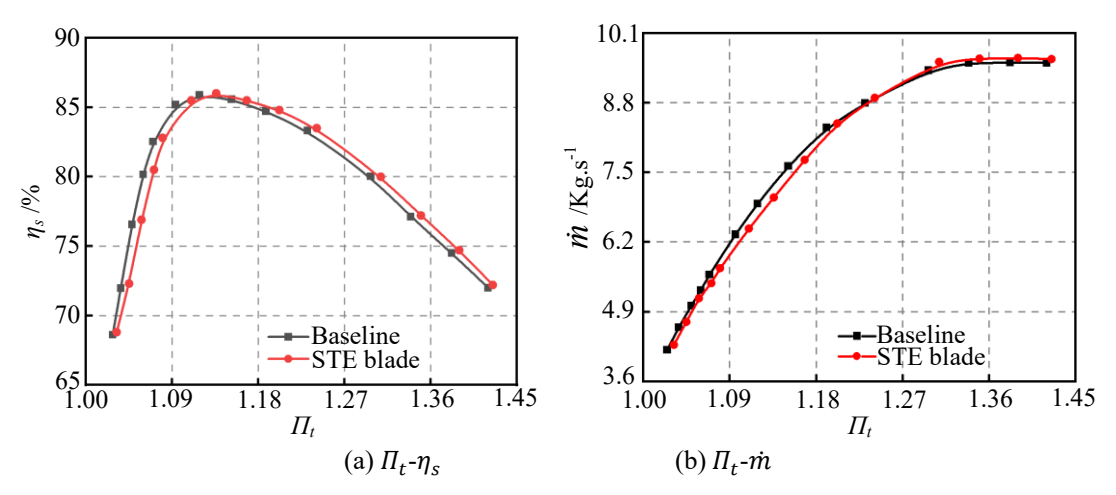


Fig. 21 Characteristic curves of the baseline and STE blades

displayed mild fluctuations due to the inherent unsteadiness of the flow, yet they remained within stable bounds throughout the calculation. The RMS values of both sets of equations (mass/momentum and turbulence) remained controlled and did not diverge, suggesting that the unsteady solution remained numerically stable. These results confirmed that the simulation results were sufficiently accurate for subsequent aerodynamic and acoustic evaluations of the biomimetic blade configurations.

Figure 21 presents the turbine characteristic curves for the baseline and STE blades. With the application of the STE blades, an increase in  $\dot{m}$  was observed in the low expansion ratio range  $(1.03 \le \Pi_t \le 1.11)$ . In the high expansion ratio range  $(1.33 \le \Pi_t \le 1.43)$ , the flow approached a critical state in which the influence of the STE blade stabilized while  $\Pi_t$  continued to increase. At the design operating point, the STE blade resulted in a 0.9% increase in  $\dot{m}$ , a 1.2% increase in  $\Pi_t$ , and a 0.9% improvement in  $\eta_s$ . The analysis confirmed that the STE blade expanded the effective flow range through the turbine while maintaining efficiency.

The primary objective of this study was to analyze the internal flow characteristics of the STE blade, including the vortex formation, wake interactions, and flow separation. Additionally, the effect of the STE blade on the

vortex intensity and aerodynamic losses was investigated in comparison to a baseline rotor. The results demonstrated that the DES method effectively addressed the unsteady flow phenomena and could be used to quantify the aerodynamic improvements produced by the STE blade (Gritskevich et al., 2012). DES is a hybrid turbulence modeling approach that combines RANS for near-wall modeling and Large Eddy Simulation (LES) for the solving of large-scale unsteady structures in separated flow regions. The governing equations in DES are derived from the N-S equations and incorporate a hybrid turbulence model:

# (i) RANS Governing Equations

$$\frac{\partial \overline{\rho}}{\partial t} + \frac{\partial}{\partial x_i} \left( \overline{\rho} \overline{u}_i \right) = 0 \tag{5}$$

$$\frac{\partial(\overline{\rho u_i})}{\partial t} + \frac{\partial}{\partial x_j} \left( \overline{\rho u_i} \overline{u_j} \right) = -\frac{\partial \overline{p}}{\partial x_i} + \frac{\partial}{\partial x_j} \left[ \mu \left( \frac{\partial \overline{u_i}}{\partial x_j} + \frac{\partial \overline{u_j}}{\partial x_i} \right) - \overline{\rho u_i' u_j'} \right]$$
 (6)

The Reynolds stress term  $\overline{u'_l u'_j}$  is modeled using turbulence closure schemes.

# (ii) LES Governing Equations

$$\frac{\partial \rho}{\partial t} + \frac{\partial}{\partial x_i} \left( \rho u_i \right) = 0 \tag{7}$$

$$\frac{\partial(\rho u_i)}{\partial t} + \frac{\partial}{\partial x_j} \left(\rho u_i u_j\right) = -\frac{\partial p}{\partial x_i} + \frac{\partial}{\partial x_j} \left[\mu \left(\frac{\partial u_i}{\partial x_j} + \frac{\partial u_j}{\partial x_i}\right) - \tau_{ij}\right]$$
(8)

The sub-grid scale stress  $\tau_{ij}$  is modeled to represent the effect of the unresolved turbulence.

(iii) The equation of energy conservation:

$$L_{t} = \min(L_{RANS}, C_{DES}\Delta) \tag{9}$$

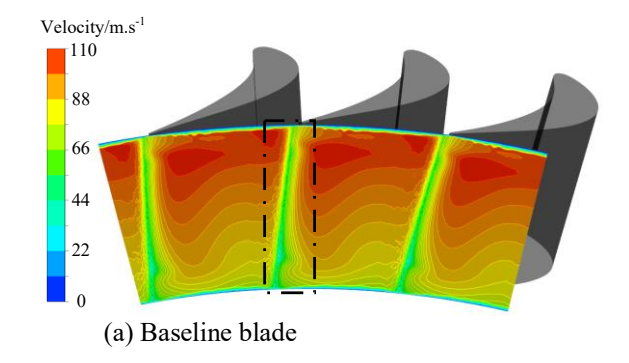
The DES model distinguishes between RANS and LES regions based on the turbulence length scale  $L_t$ . The  $L_{RANS}$  is the turbulence length scale derived from the RANS model,  $\Delta$  is the local grid spacing, and  $C_{DES}$  is a calibration constant.

The Detached Eddy Simulation (DES) utilized in this study was based on the standard k– $\varepsilon$  model in the RANS regions and transitioned to LES behavior in separated flow zones, with the default subgrid-scale (SGS) model constants as implemented in CFX, including a Smagorinsky coefficient of 0.1. The near-wall regions were resolved using low-Re wall treatment with a first-layer y<sup>+</sup><1 to accurately capture the viscous sublayer. A constant time step of  $4.2\times10^{-6}$  s was used, corresponding to approximately 408 time steps per rotor revolution at 3500 rpm. This choice maintained the Courant number (CFL) below one in the critical regions, ensuring numerical stability and adequate resolution of unsteady turbulence structures and acoustic features such as rotor-stator interaction and wake vortex shedding.

Figure 22 presents the velocity distribution on the radial plane (at a location 3 mm downstream of the rotor trailing edge) at the rotor exit, where a distinct velocity difference is observed between the wake and the main flow regions. The main flow exhibited a higher velocity, while the wake region was characterized by a lower velocity. As the airflow passed through the blade passage, the STEs enhanced the mixing between the wake and the main flow, particularly near the serration root. The premature mixing of the high-pressure flow from the pressure side and the low-pressure flow from the suction side resulted in a velocity distribution at the blade exit that exhibited a serrated pattern. The presence of the serrations not only improved the wake structure but also contributed to a more uniform velocity gradient in the main flow region.

Figure 23 presents the streamline distribution at the serration location. Due to the interference induced by the serrated geometry, local flow separation occurred in the mainstream near the serration root region. As the fluid passed through the root, it reattached to the separated flow region, causing the streamlines to distort and reconnect. This process resulted in a more complex streamline pattern near the root. The mixing effect between the mainstream and the wake was enhanced in this region, leading to the stretching and curvature of the streamlines.

As shown in Fig. 24(a), the pressure gradient along the pressure surface remained relatively uniform, and the pressure variation in the trailing-edge region was smooth, with no significant fluctuations. In contrast, a periodic pressure variation was observed at the serration region,



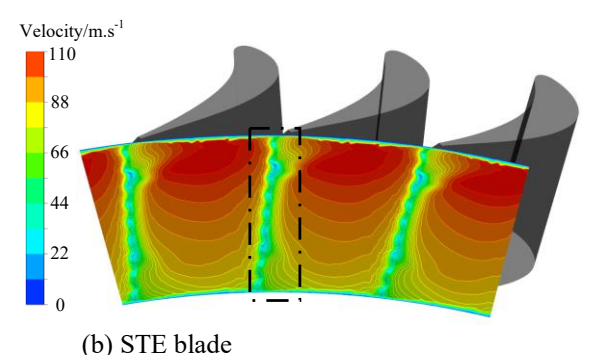


Fig. 22 Velocity distribution of the radial plane at the rotor outlet

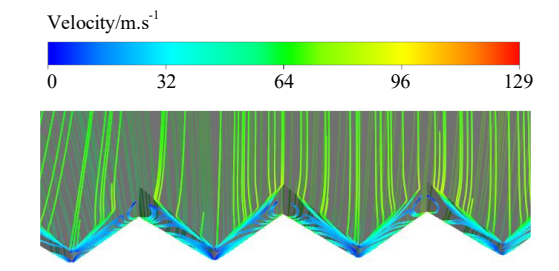


Fig. 23 Streamline distribution at the serration location

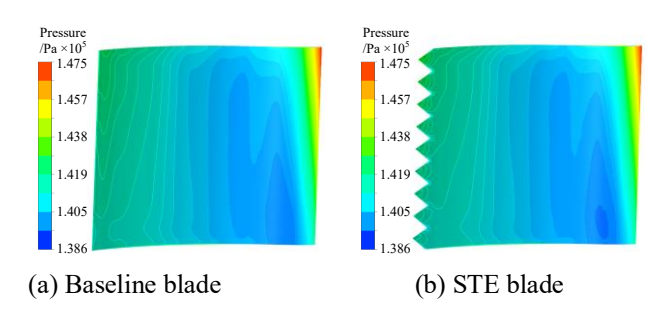


Fig. 24 Pressure distribution of the rotor blades

which reduced the wake concentration and resulted in a more uniform mean pressure distribution at the trailing edge. At the serration tip, the local pressure was slightly higher than that at the serration root, which was attributed to the flow separation and reattachment induced by the serration geometry. Near the serration root, the enhanced mixing between the freestream and wake led to a slightly lower pressure compared to the corresponding baseline location.

Figure 25 presents a comparison of the surface static pressure distributions between the STE blade and baseline

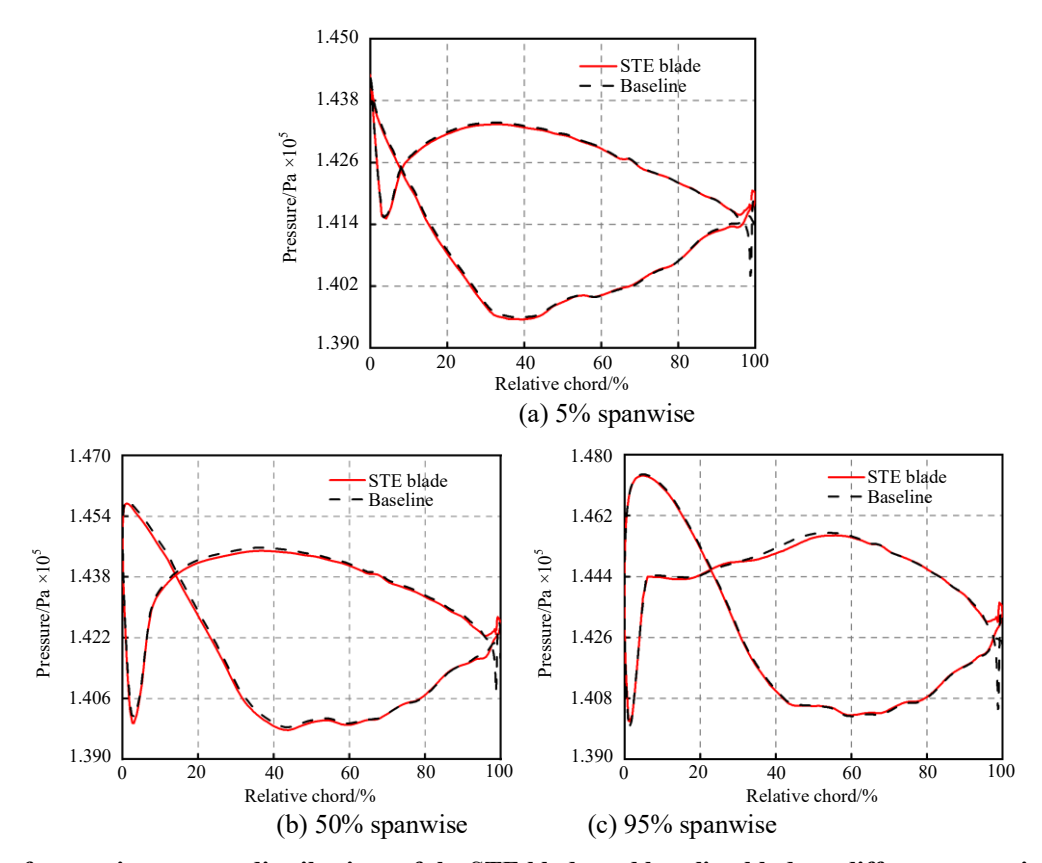


Fig. 25 Surface static pressure distributions of the STE blade and baseline blade at different spanwise locations

blade at different spanwise locations. Overall, a similar trend was observed for both blades, while a more gradual pressure variation was detected near the trailing edge of the STE blade compared to the baseline blade. This indicated that the serrated structure effectively reduced the pressure gradient at the trailing edge, leading to a more uniform wake and mitigating the unsteady flow instabilities, thereby contributing to aerodynamic noise reduction.

Figure 26 illustrates the vortex structure evolution of the STE blade at different time steps. The main mechanisms observed included the separation, mixing, and redistribution of the vortices, with the vortex distribution analyzed using the *Q*-criterion ( $Q=5.87\times10^5$  s<sup>-</sup> <sup>2</sup>). As shown in Fig. 26(a), vortex cores were formed at the serration valleys, and due to the small serration size, the vortex cores exhibited a continuous distribution. Figure 26(b) indicates that as the airflow interacted with the STE, the flow separated along both sides of the serration, and vortex structures were generated between the serration peaks and valleys. This indicated that the separation pattern of the shear layer was modified by the serration, causing the vortices to shed primarily from both sides of the serration. As shown in Fig. 26(c), a vortex tube was formed by the mixing of the vortices downstream of the separation region. The streamwise vortex distribution at the STE blade trailing edge exhibited improved uniformity in both size and orientation. The vortices remained nearly parallel and independent, with a spacing approximately equal to the serration wavelength. The formation of these vortices was primarily attributed to flow direction disturbances caused by the trailing edge geometry, which forced the airflow to periodically separate and rotate into

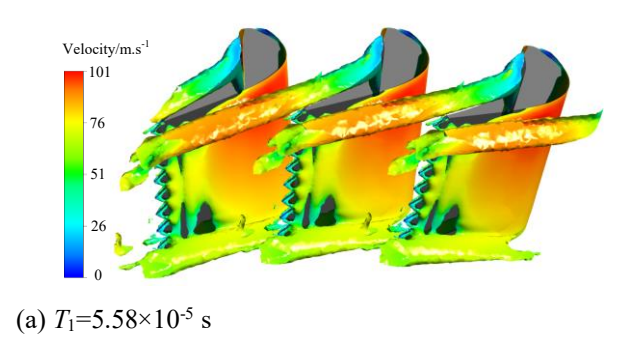
vortex structures. These vortices gradually dissipated along the flow direction.

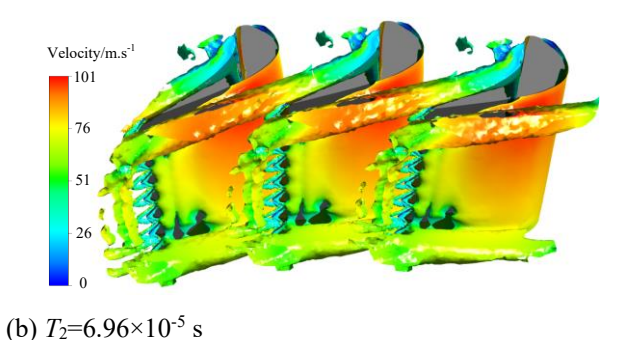
# 4. AEROACOUSTIC PERFORMANCE OF STE BLADE

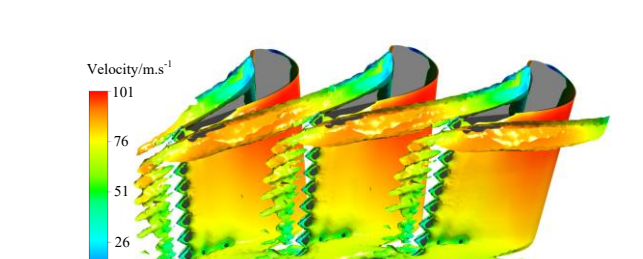
# 4.1 Time-Domain Distribution of the Static Pressure for the Baseline and STE Blades

The turbine noise was primarily generated by the propagation of pressure fluctuations caused by the trailing edge vortices of the rotor blades. As shown in Fig. 27, these vortices were identified as the main source of the unsteady pressure fluctuations that contributed significantly to the aerodynamic noise.

To investigate the unsteady flow mechanisms associated with aerodynamic noise generation, monitoring points were positioned at 20%, 50%, and 80% spanwise locations on the rotor blade, as shown in Fig. 28. Figure 29 illustrates the time-domain distribution of the static pressure for different spanwise locations under design flow conditions for the baseline blade. This periodic behavior was primarily induced by the interaction between the rotor blades and the airflow. The pulsation amplitude near the blade root was significantly lower than that at the tip, indicating that the root region was constrained by the casing and hub. This resulted in a relatively stable flow and weaker pressure fluctuations. In contrast, the flow exhibited greater complexity and was strongly influenced by secondary flows at the blade tip. This led to larger pressure fluctuations, which served as an energy source for aerodynamic noise generation.







(c)  $T_3 = 8.34 \times 10^{-5} \text{ s}$ 

Fig. 26 Vortex structures of the STE blade at different time steps

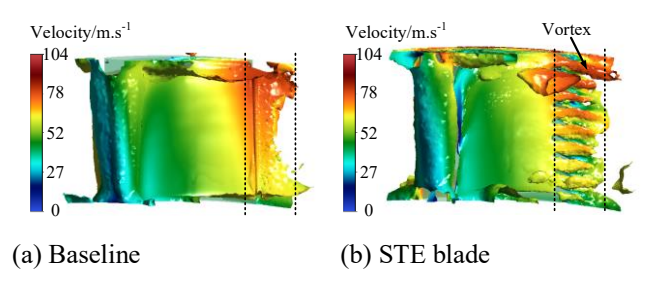


Fig. 27 Trailing edge vortices of the blades

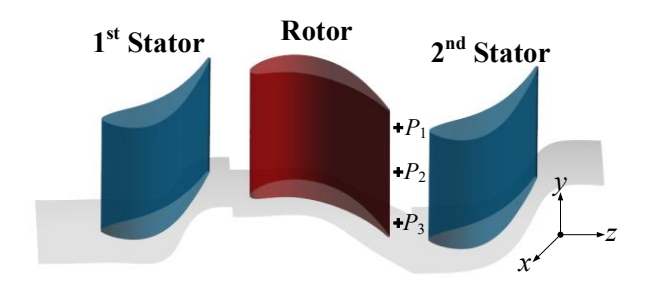


Fig. 28 Arrangement of monitoring probes

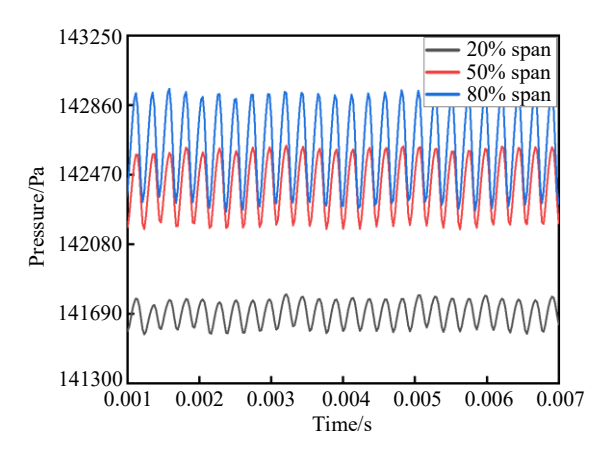


Fig. 29 Time-domain distribution of the static pressure for the baseline blade

Figure 30 presents the time-domain distribution of the static pressure fluctuations at 20%, 50%, and 80% spanwise locations for both the baseline and STE blades. The results indicated that distinct periodic variations occurred at each monitoring point, with a cycle period of approximately  $4.2 \times 10^{-4}$  s, corresponding to the blade passing frequency (BPF) of the rotor. At 20% spanwise, the mean static pressure was relatively low, with the smallest fluctuation amplitude and a peak-to-valley pressure difference of approximately 199.44 Pa. At 50% spanwise, the mean static pressure was slightly higher than that at the root, with an increased fluctuation amplitude and a peak-to-valley difference of 444.88 Pa. This indicated a stronger influence of unsteady flow structures. At 80% spanwise, the mean static pressure reached its highest value, and the fluctuation amplitude significantly increased, with a peak-to-valley difference of 674.92 Pa. This suggested that the blade tip region was strongly affected by secondary flows, leading to intensified pressure fluctuations. At all spanwise locations, the pressure fluctuations of the STE blade remained lower than those of the baseline blade, with the most significant attenuation observed at the 80% span. This indicated that the pressure disturbances were mitigated by the STE blade.

### 4.2 Aeroacoustics of Baseline and STE Blades

In this study, the trailing edge fluctuating pressure of rotor blades is considered as the primary noise source (Ye et al., 2022a), and Computational Aeroacoustics (CAA) is employed to predict the radiated noise. The static pressure fluctuations were converted into the frequency domain using the FFT (Ghasemian & Nejat, 2015). The time-resolved surface pressure signal p(t) was transformed into the frequency domain using FFT, yielding the pressure spectrum P(f) as shown in formula (10). The spectrum P(f) characterizes the distribution of pressure fluctuation energy across the frequencies, and reveals tonal components such as the BPF and its harmonics, which are indicative of aerodynamic noise sources.

$$P(f) = \left| \sum_{n=0}^{N-1} p(t_n) \times e^{-j2\pi f t_n} \right|$$
 (10)

where  $p(t_n)$  denotes the pressure value at the *n*-th time sample in the time domain, and P(f) represents the spectral amplitude at frequency f.

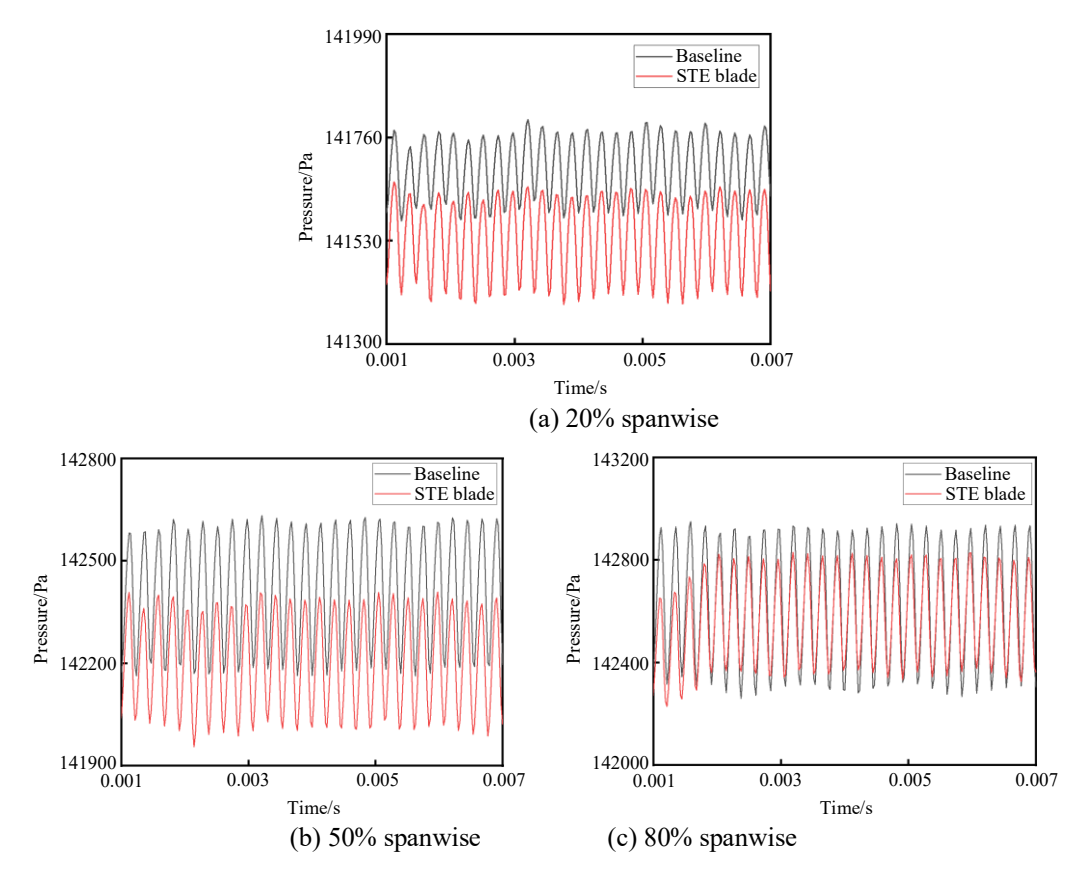


Fig. 30 Time-domain distribution of the static pressure for the baseline and STE blades at different spanwise

To convert these pressure fluctuations into acoustic metrics, the FFT was applied to transform the time-domain pressure signals into the frequency domain. The resulting pressure spectra were then used to calculate the sound pressure level (SPL) using the formula (11) (Ye et al., 2022b; Kim et al., 2021).

$$SPL = 20 \times \log_{10} \frac{P_{st}}{P_0}$$
 (11)

Where  $P_{st}$  is the instantaneous pressure at the monitoring point and  $P_0 = 20\mu\text{Pa}$  is the reference sound pressure in air.

The resulting noise spectrum is presented in Fig. 31. Distinct pressure peaks were observed at the BPF and its harmonics. Due to the relatively stable flow field near the blade root, lower pressure fluctuation amplitudes were obtained, leading to weaker aerodynamic excitation. As a result, the SPL at the BPF and its harmonic frequencies was lower in the blade root region compared to the blade tip.

As the blade passed the monitoring point, periodic variations in the fluid pressure and velocity were induced, generating BPF noise and its harmonic components. The BPF was calculated using the following equation (Mahmoodi & Montazerin, 2020):

$$f = \frac{Zn}{60} \tag{12}$$

where Z is the number of rotor blades and n is the rotational speed. The BPF of the turbine was calculated to be 2391.67 Hz.

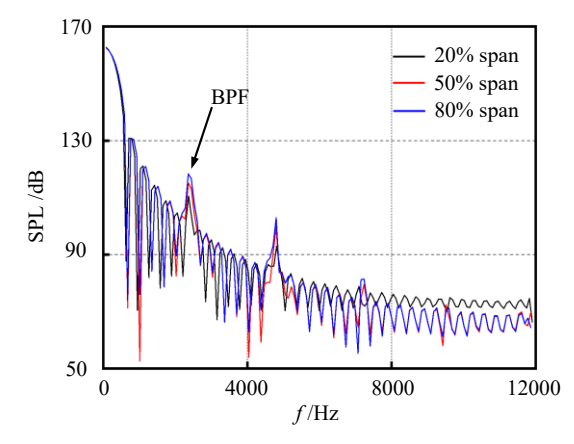


Fig. 31 SPL distribution at each probe for the baseline blade

Figure 32 presents the spectra of the SPL at 20%, 50%, and 80% spanwise locations for both the baseline and STE blades. A distinct SPL peak was observed at the BPF. Compared to the baseline blade, a significant reduction in the SPL was achieved with the STE blade at all spanwise positions, demonstrating the STE blade's effectiveness in mitigating the periodic noise induced by the blade-flow interactions. In the low-frequency range (f<2391.67 Hz), broadband noise was primarily generated by large-scale flow structures and secondary flow interactions. At all spanwise locations, a notable reduction in the noise was observed with the STE blade, indicating that the largescale turbulence structures were weakened. This led to a decrease in the flow-induced noise. In the mid-to-high frequency range (f>2391.67 Hz), the noise was predominantly caused by boundary layer instabilities and

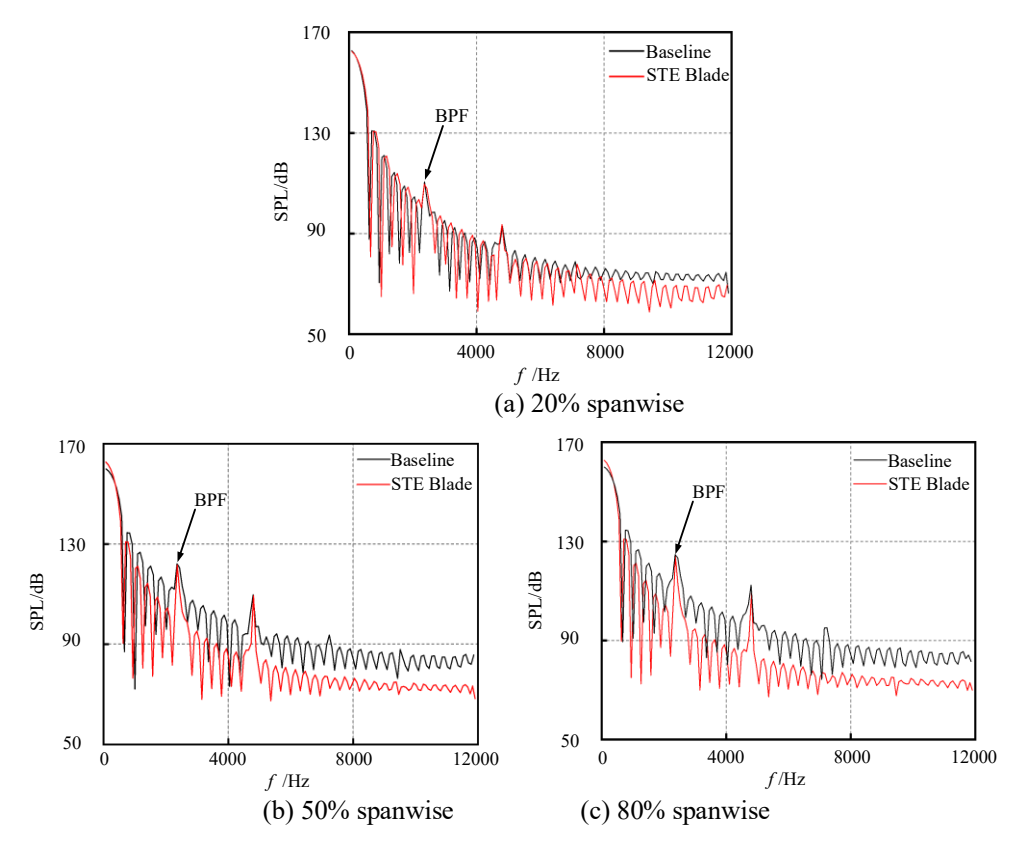


Fig. 32 Distribution of SPL for the baseline and STE blades at different spanwise locations

trailing-edge vortex shedding. Flow instabilities were effectively suppressed by the STE blade, resulting in a significant reduction in the high-frequency noise. Specifically, above 8000 Hz, where the fine-scale turbulence and trailing-edge noise dominated, superior noise attenuation was achieved with the STE blade. At the 80% spanwise location, the most pronounced noise reduction was observed. Compared with the baseline blade, the SPL of the STE blade was decreased by approximately 8.52 dB in the low-frequency range and 12.49 dB in the high-frequency range. These results confirmed that periodic pressure fluctuations were effectively weakened turbulence-induced noise was significantly suppressed by the STE blades. This provides a foundation for the further optimization of low-noise blade designs.

# 5. CONCLUSION

In this study, the wake disturbances and vortex structures of STE rotor blades were investigated utilizing rotor-stator interaction effects. DES was employed to analyze the impact of the STE on the wake dynamics. Additionally, noise reduction mechanisms were examined by evaluating static pressure fluctuations at the trailing edge. The key findings were as follows:

(1) The STE promoted early mixing between the highpressure flow from the pressure side and the low-pressure flow from the suction side, thereby reducing the wake velocity deficits. Furthermore, the streamwise vortex distribution at the trailing edge of the STE blade exhibited improved uniformity in both size and orientation. The vortices remained nearly parallel and independent, with a spacing that was approximately equal to the serration wavelength.

- (2) Flow reattachment occurred at the serration root due to geometric-induced perturbations, leading to the reconnection of separated flow regions. This process distorted and realigned the streamlines, enhancing the mixing effect between the freestream and wake regions.
- (3) Compared with the baseline blade, the pressure fluctuations at the trailing edge were effectively suppressed by the effect of the STE blade. Consequently, SPL reductions were achieved of approximately 8.52 dB in the low-frequency range and 12.49 dB in the high-frequency range

In future work, the optimization of serration geometries—including spanwise variations in the amplitude and wavelength—will be explored to further improve aerodynamic and acoustic performance. In addition, an acoustic propagation model will be further established, and far-field acoustic predictions will be considered to better correlate near-field SPL results with far-field noise behavior. Additionally, experimental tests will be developed to support the numerical findings and enhance the engineering applicability of STE designs.

### **ACKNOWLEDGEMENTS**

This work was supported by the National Natural Science Foundation of China (Grant No. 52205116), the Doctoral Research Initiation Project of Liaoning Province Natural Science Foundation (Grant No. 2024-BS-157), the Education Department Project of Liaoning Province (Grant No. JYTMS20230258), the Foundation of the Key Laboratory of Rapid Development and Manufacturing Technology for Aircraft (Grant No. LJ232410143008) and Foundation of the State Key Laboratory for Aviation

Digital Manufacturing Processes (Grant No. SHSYS202406).

#### **CONFLICTS OF INTEREST**

The authors declare that they have no known competing financial interests or personal relationships that could have appeared to influence the work reported in this paper.

### **AUTHORS CONTRIBUTION**

**D. D. Sui:** Formal analysis, Visualization, Writing—original draft; **W. J. Yang:** Conceptualization, Methodology, Formal analysis, Supervision, Resources, Writing—review and editing; **X. P. Wang:** Formal analysis, Visualization, Data curation; **Y. H. Wang:** Visualization, Data curation; **Y. Z. Zhang:** Formal analysis, Data curation.

#### REFERENCES

- Ahmadkhah, S., Jahangirian, A., & Zarinvafa, A. (2025).

  Aerodynamic Performance of Different Trailing-edge Serrations for High Reynolds Number Flows around Wing-flap System. *Journal of Applied Fluid Mechanics*, 18(4), 1035-1047.

  <a href="https://doi.org/10.47176/jafm.18.4.2936">https://doi.org/10.47176/jafm.18.4.2936</a>
- Alawadhi, H. A., Alex, A. G., & Kim, Y. H. (2014). CFD analysis of wing trailing edge vortex generator using serrations. *EPJ Web of Conferences*, *67*, 02002. <a href="https://doi.org/10.1051/epjconf/20146702002">https://doi.org/10.1051/epjconf/20146702002</a>
- Aubé, M., & Hirsch, C. (2001). Numerical investigation of a 1-1/2 axial turbine stage at quasi-steady and fully unsteady conditions. In *Proceedings of the ASME Turbo Expo: Power for Land, Sea, and Air, 1*, V001T03A013. <a href="https://doi.org/10.1115/2001-GT-0309">https://doi.org/10.1115/2001-GT-0309</a>
- Chandra, S., & Sharma, S. D. (2017). An experimental investigation to enhance the aerodynamic efficiency of micro aerial vehicle wing using bio-inspired serrations. *International Journal of Aeronautical and Space Sciences*, 22(5), 1042-1047. https://doi.org/10.1007/s42405-021-00388-6
- Chen, H., Li, L., Liu, H., & Yu, M. (2018). Redesign and wake flow field for a compressor high-turning stator with bifurcate blade. *Journal of Aerospace Power*, 33(6), 1381-1392. https://doi.org/10.13224/j.cnki.jasp.2018.06.012
- Chong, T., & Vathylakis, A. (2015). On the aeroacoustic and flow structures developed on a flat plate with a serrated sawtooth trailing edge. *Journal of Sound & Vibration*, 354(10), 65-90. https://doi.org/10.1016/j.jsv.2015.05.019
- Feng, W., Chen, K., Gui, H., Zhao, P., Gao, R. & Li, Y.
  (2023). Aerodynamic Noise Reduction Based on Bionic Blades with Non-Smooth Leading Edges and Curved Serrated Trailing Edges. *Journal of Applied* Fluid Mechanics, 16(7), 1402-1413.

## https://doi.org/10.47176/jafm.16.07.1660

- Ghasemian, M., & Nejat, A. (2015). Aerodynamic noise prediction of a horizontal axis wind turbine using improved delayed detached eddy simulation and acoustic analogy. *Energy Conversion and Management*, 99(15), 210-220. https://doi.org/10.1016/j.enconman.2015.04.011
- Gritskevich, M. S., Garbaruk, A. V., Jochen Schütze, & Menter, F. R. (2012). Development of DDES and IDDES formulations for the k-ω shear stress transport model. *Flow, Turbulence and Combustion*, 88(3), 431-449. <a href="https://doi.org/10.1007/s10494-011-9378-4">https://doi.org/10.1007/s10494-011-9378-4</a>
- Gruber, T., Murray, M. M., & Fredriksson, D. W. (2011). Effect of Humpback Whale Inspired Tubercles on Marine Tidal Turbine Blades. In *Proceedings of the Asme International Mechanical Engineering Congress and Exposition*,851-857. <a href="https://doi.org/10.1115/IMECE2011-65436">https://doi.org/10.1115/IMECE2011-65436</a>
- Hodson, H. P., & Howell, R. J. (2005a). Bladerow interactions, transition, and high-lift aerofoils in low-pressure turbines. *Annual Review of Fluid Mechanics*, 37(1), 71-98. <a href="https://doi.org/10.1146/annurev.fluid.37.061903.17">https://doi.org/10.1146/annurev.fluid.37.061903.17</a>
- Hodson, H. P., & Howell, R. J. (2005b). The role of transition in high-lift low-pressure turbines for aeroengines. *Progress in Aerospace Sciences*, 41(6), 419-454. https://doi.org/10.1016/j.paerosci.2005.08.001
- Howe, M. S. (1991). Aerodynamic noise of a serrated trailing edge. *Journal of Fluids and Structures*, 5(1), 33-45. <a href="https://doi.org/10.1016/0889-9746(91)80010-B">https://doi.org/10.1016/0889-9746(91)80010-B</a>
- Hu, J. G., Wang, R. G., & Huan, D. Q. (2019). Improvements of performance and stability of a single-stage transonic axial compressor using a combined flow control approach. *Aerospace Science and Technology*, 86, 283-295. <a href="https://doi.org/10.1016/j.ast.2018.12.033">https://doi.org/10.1016/j.ast.2018.12.033</a>
- Kim, D., Safdari, A., & Kim, K. C. (2021). Sound pressure level spectrum analysis by combination of 4D PTV and ANFIS method around automotive side-view mirror models. *Scientific Reports*, 11(1), 11155. <a href="https://doi.org/10.1038/s41598-021-90734-1">https://doi.org/10.1038/s41598-021-90734-1</a>
- Launder, B. E. (1974). The numerical computation of turbulent flows ScienceDirect. *Computer Methods in Applied Mechanics and Engineering*, 3(2), 269-289. https://doi.org/10.1016/0045-7825(74)90029-2
- Lee, S., Ayton, L., Bertagnolio, F., Stéphane Moreau, & Joseph, P. (2021). Turbulent boundary layer trailing-edge noise: theory, computation, experiment, and application. *Progress in Aerospace Sciences*, *126*(1), 100737. https://doi.org/10.1016/j.paerosci.2021.100737
- Li, C. X., Zhang, C., Zhang, R. X., & Ye, X. M. (2020). Effect of Gurney flap on performance and

- aeroacoustics of variable-pitch axial fans. AIAA Journal, 58(6), 2546-2559. https://doi.org/10.2514/1.J059192
- Li, G., Zhang, G., He, H., Zhao, C., Zhao, Z., & Zhang, W. (2024). Coupling Effect of Particle Deposition Inside and Outside Holes on Film Cooling Performance on the Leading Edge of the Blade. Journal of Applied Fluid Mechanics, 17(10), 2192-2202. https://doi.org/10.47176/jafm.17.10.2539
- Liu, B. J., Zhang, C. H., An, G. F., Fu, D., & Yu, X. J. (2022). Using tandem blades to break loading limit of highly loaded axial compressors. Chinese Journal Aeronautics, 35(4), 165-175. https://doi.org/10.1016/j.cja.2021.07.031
- Liu, C., Cao, Y., Zhang, W., Ming, P., & Liu, Y. (2019). Numerical and experimental investigations of compressor BPF centrifugal noise. Applied 290-301. Acoustics, 150, https://doi.org/10.1016/j.apacoust.2019.02.017
- Maciej, K., & Blaszczak, J. (2008). Performance of Three Turbulence Models in 3D Flow Investigation for a 1.5-Stage Turbine. *Task quarterly*. 12(3), 185-195. https://journal.mostwiedzy.pl/TASKQuarterly/articl e/view/2033
- Mahmoodi, M., & Montazerin, N. (2020). On the Aerodynamic and Acoustic Behavior of Double Outlet Squirrel Cage Fans. Journal of Applied Fluid Mechanics, 13(6), 1873-1883. https://doi.org/10.47176/jafm.13.06.31248
- Manabe, K., Ito, S., Furukawa, M., Yamada, K., Oka, N., & Tomita, I. (2019). Simultaneous optimization of impeller blade loading distribution and meridional geometry for aerodynamic design of centrifugal compressor. ASME/JSME/KSME Joint Fluids Conference. Engineering https://doi.org/10.1115/AJKFluids2019-5358
- Meyer, R. (1958). The effect of wakes on the transient pressure and velocity distributions in turbomachines. Journal of **Fluids** Engineering. https://doi.org/10.1115/1.4012797
- Naeini, H. K., Nili-Ahmadabadi, M., & Kim, K. C. (2019). An experimental study on the effect of a novel nature inspired 3D-serrated leading edge on the aerodynamic performance of a double delta wing in the transitional flow regime. Journal of Mechanical Science and Technology, 33(12), 5913-5921. https://doi.org/10.1007/s12206-019-1136-x
- Rona, A., & Gostelow, J. P. (2005). Performance of Slotted End Wall Linear Cascade Tunnels at Off-

- design Conditions. In Proceedings of the 43rd AIAA Aerospace Sciences Meeting and Exhibit.1-12. https://doi.org/10.2514/6.2005-908
- Walraevens, R. E., Gallus, H. E., Jung, A. R., Jürgen F. Mayer, & Stetter, H. (1998). Experimental and computational study of the unsteady flow in a 1.5 stage axial turbine with emphasis on the secondary flow in the second stator. The American Society of Mechanical Engineers. 1-15. https://doi.org/10.1115/98-GT-254
- Wissink, J. G., Rodi, W., & Hodson, H. P. (2006). The influence of disturbances carried by periodically incoming wakes on the separating flow around a turbine blade. International Journal of Heat and Fluid Flow, 27(4), 721-729. https://doi.org/10.1016/j.ijheatfluidflow.2006.02.01
- Yang, W. J., Sui, D. D., Wang, X. P., Gao, X., & Wang, L. (2025a). Wake control of aeroengine blade based on matching design of the non-uniform serrations. Proceedings of the Institution of Mechanical Engineers, Part G: Journal of Aerospace Engineering, 1-16. https://doi.org/10.1177/09544100251350345
- Yang, W. J., Sui, D. D., Wang, Y. H., & Zhan, Y. D. (2025b). Flow control and noise reduction of axial compressor based on stator blade design with the non-uniform serrations. Physics of Fluids, 37(7), 075176. https://doi.org/10.1063/5.0278049
- Ye, X., Zheng, N., Hu, J., Li, C., & Xue, Z. (2022a). Numerical investigation of the benefits of serrated gurney flaps on an axial flow fan. Energy, 252, 124072.
  - https://doi.org/10.1016/j.energy.2022.124072
- Ye, X., Zheng, N., Zhang, R., & Li, C. (2022b). Effect of serrated trailing-edge blades on aerodynamic noise of an axial fan. Journal of Mechanical Science and Technology, 36. 2937-2948. https://doi.org/10.1007/s12206-022-0526-7
- Yildiz, E., Koca, F., & Can, I. (2024). Optimal Design and Analysis of the Cooled Turbine Blade in Gas Turbines with CFD. Journal of Applied Fluid 18(1), 60-72. Mechanics, https://doi.org/10.47176/jafm.18.1.2853
- Yuan, S., Wu, Y., Zhao, S., Lu, X., & Han, G. (2024). Investigation on the aerodynamic performance and flow mechanism of transonic ultra-highly loaded tandem-rotor stage. Aerospace, 11(5),https://doi.org/10.3390/aerospace11050389